Laboratory study of the collection efficiency of submicron aerosol particles by cloud droplets.
Part II - Influence of electric charges.

Alexis Dépée [1,2], Pascal Lemaitre[1*], Thomas Gelain[1], Marie Monier[2,3], Andrea Flossmann[2,3]

[1] {Institut de Radioprotection et de Sûreté Nucléaire (IRSN), PSN-RES, SCA, Gif-sur-Yvette, France}

[2] {Université Clermont Auvergne, Laboratoire de Météorologie Physique, Clermont-Ferrand, France}

[3] {CNRS, INSU, UMR 6016, LaMP, Aubière, France}

*Correspondence to: Pascal Lemaitre (pascal.lemaitre@irsn.fr)

ABSTRACT

A new In-Cloud Aerosol Scavenging Experiment (In-CASE) has been developed to measure the collection efficiency (CE) of submicron aerosol particles by cloud droplets. Droplets fall at their terminal velocity through a one-meter-high chamber in a laminar flow containing aerosol particles. At the bottom of the In-CASE's chamber, the droplet train is separated from the aerosol particles flow and the droplets are collected in an impaction cup whereas aerosol particles are deposited on a High Efficiency Particulate Air (HEPA) filter. The collected droplets and the filter are then analysed by fluorescence spectrometry since the aerosol particles are atomised from a sodium fluorescein salt solution ($C_{20}H_{10}Na_2O_5$). In-CASE fully controls all the parameters which affect the CE - the droplets and aerosol particles size distributions are monodispersed, the electric charges of droplets and aerosol particles are known and set, while the relative humidity is indirectly controlled via the chamber's temperature. This paper details the In-CASE setup and the dataset of 70 measurements obtained to study the impact of the electric charges on CE. For this purpose, droplets and particles charges are controlled through two charging systems developed in this work - both chargers are detailed below. The droplet charge varies from $-3.0 \times 10^4 \pm 1.4 \times 10^3$ to $+9.6 \times 10^4 \pm 4.3 \times 10^3$ elementary charges while the particle charge ranges from the neutralisation to -90 ± 9 elementary charges depending on the particle radius. A droplet radius of 48.5 ± 1.1 µm has been considered for four particle dry radii between 100 and 250 nm. These new CE measurements have been compared to the correlation of Kraemer and Johnstone (1955) and the extended model of Dépée et al. (2019) where thermophoresis and diffusiophoresis are also considered since the measurements have been performed at a relative humidity level of 95.1 ± 0.2 %. As a result, both models adequately describe the electric charge influence on the measured CEs. Furthermore, the effect of the image charge (Jackson, 1999) in the electrostatic forces is measured.

INTRODUCTION

Aerosol particles (APs) are a fundamental part of the atmosphere since they act on climate and more locally on meteorology (Twomey et al., 1974). They are also a key topic in human health where APs increase the likelihood of developing cardiovascular disorder (Crouse et al., 2012). For these reasons, the processes involved in the removing of the atmospheric AP have been investigated extensively over the last decades. Far away from the source, APs are mainly scavenged through their collection by clouds and precipitations (Jaenicke, 1993) - referred as the wet deposition. Since it has been reported that the AP collection by clouds prevails in the wet deposition (Flossmann, 1998 ; Laguionie et al., 2014), the modelling of the in-cloud AP collection remain an essential issue for the atmospheric sciences.

As previously stated in Part I of this work (**Dépée et al., 2020**) – « In most of current AP wet removal models - like DESCAM (Detailed SCAvenging Model, Flossmann, 1985) - the AP collection is described through a microphysical parameter called "collection efficiency" (CE) which quantifies the ability of a droplet to capture the APs present in its surroundings during its fall. Many microphysical effects impact this CE and their contribution is mainly depending on the AP size. To be collected an AP has

50 to leave the streamline that surrounds the falling droplet to make contact with it. The nanometric
51 AP's motion is affected by the collisions with air molecules - referred as the Brownian diffusion. It
52 results in random movement patterns (see Figure 1, A) which tend to increase the CE as the AP radius
53 decreases. For massive APs, there is an increase of CE as they retain an inertia strong enough to leave
54 the streamline when it curves and to go straight toward the droplet surface - phenomenon called
55 inertial impaction (see Figure 1, B). When considering intermediate AP size, the CE goes through a
56 minimum value called the "Greenfield gap" (Greenfield, 1957) where the AP diffusion and inertia are
57 weaker. In this gap, other microphysical effects can be involved to make the droplet encounter the
58 AP like the interception, for instance. It is the collection of APs following a streamline that
59 approaches the droplet within a distance equivalent to the particle radii (a) - see Figure 1, C. ». Note
60 that there are also thermophoretic and diffusiophoretic forces which can have an influence on the
61 CE. These effects prevail in a subsaturated air - as it is the case sometimes in clouds - and are
62 discussed in Part I (**Dépée et al., 2020**).
63 Since droplets are naturally charged in clouds (Takahashi, 1973) as well as the atmospheric APs, there
64 are electrostatic forces which can influence the AP collection. Numerous numerical studies were
65 dedicated to the influence of the electric charges on CE – such as Grover et al. (1975), Jaworek et
66 al. (2002), Tinsley and his group (for instance - Tinsley et al., 2006 or Tinsley and Zhou, 2015). They
67 suggest an increase of the CE of several orders of magnitude even when the AP is weakly charged.
68 However, the AP charge increases when the APs are radioactive (Clement and Harrison, 1992) -
69 inducing an impact on CE even larger (Dépée et al., 2019). Thus, the AP "electroscavenging" in clouds
70 has to be investigated, particularly for nuclear safety issues when the APs removal by clouds result
71 from the discharge of radioactive materials from a nuclear accident. Prior, the CE values considering
72 electrostatic forces need to be compared with experiments and, more specifically, the analytical
73 expression for electrostatic forces used in numerical studies (Jaworek et al., 2002 ; Tinsley et al.,
74 2006 ; Tinsley and Zhou, 2015 ; Dépée et al., 2019) has to be confronted.
75 When a droplet with a charge Q approaches an AP of charge q, the partial influence of the AP
76 electrostatic field on the droplet leads to the re-orientation of the water dipoles. As a result, a
77 surface charge distribution on the droplet is created and supposed to be comparable to the one of a
78 conductive sphere. In an electrostatic equivalent problem, the droplet can be replaced by two-point
79 charges (Jackson, 1999). One modelling the charge distribution, inside the droplet and near its
80 surface, another for the residual droplet charge located at the droplet surface. Finally, the analytical
81 expression of the electrostatic forces is the addition of two Colomb forces between the AP and the
82 two-point charges inside the droplet. The factored expression can be found in equation 7 of Dépée
83 et al. (2019) and further details can be found in Tinsley et al. (2000). It is holds two terms (Equation
84 (6)). The first one is the Coulomb inverse square term which prevails in the AP collection for large
85 enough AP electrical mobilities or electric charge products ($q \times Q$), attractive (Figure 1, D) or
86 repulsive (Figure 1, E) depending on whether the AP charge (q) and the droplet charge (Q) have unlike
87 or like signs. The second term is referred to the short-range attractive term and dominates for weak
88 electric charge products or for small AP electrical mobilities (Figure 1, F) and is always attractive
89 (due to the charge distribution at the droplet surface with opposite sign to the AP charge (q)). A
90 detailed study of their contribution can be found in Dépée et al. (2019).
91 Several laboratory studies were also performed regarding the influence of the electric charges on the
92 CE (Beard, 1974; Wang and Pruppacher, 1977; Lai et al., 1978; Barlow and Latham, 1983; Wang et
93 al., 1983; Byrne and Jennings, 1993). However, most of these works have faced difficulties in
94 controlling all parameters impacting the CE. For instance, Beard (1974) do not measure the AP charge
95 ; Lai et al. (1978) have a polydispersed AP size distribution, the relative humidity level is not provided
96 and the terminal velocity of the droplets is not reached ; Barlow and Latham (1983) use a
97 polydispersed AP size distribution and the relative humidity level significantly varies from 50 to 70 %
98 in their measurements; in the work of Byrne and Jeannings (1993) the droplet velocity does not reach
99 the terminal velocity. For these reasons, it is really difficult to find comparable CE measurements in
100 the literature as Barlow and Latham (1983) concluded after highlighting a discrepancy of few orders
101 of magnitude between all these authors. Nevertheless, Wang and Pruppacher (1977) and Wang et al.
102 (1983) succeed in controlling the charges and the sizes (as well as the relative humidity for Wang and
103 Pruppacher (1977)) but they consider only unlike signs between both droplets and APs. Thus, only
104 the Coulomb inverse square term in the analytical expression of the electrostatic forces can be
105 documented whereas the contribution of the short-range attractive term has not been experimentally
106 verified until now.
107 The purpose of this study is to overcome this lack of data by providing new CE measurements for
108 weakly and strongly droplets and APs charges with both negative and positive charge products, to

109 quantify the effect of the short-range attractive term on the CE since its contribution was previously
110 predicted by modelling (Tinsley and Zhou, 2015; Dépée et al., 2019).
111 Thus, a novel experiment has been designed for this study. With this experiment, the influence of
112 relative humidity can also be investigated and this was the object of the companion paper of this
113 present work : Part I **(Dépée et al., 2020)**.
114 In the first section of this paper, Part II, the experimental setup is detailed while the experimental
115 method to evaluate the CE is described in the second one. Then, the measurements are presented
116 and confronted with the correlation of Kraemer and Johnstone (1955) which accounts for attractive
117 Coulomb interactions between droplets and APs. Another comparison is made in the last section with
118 the Lagrangian model of Dépée et al. (2019) which provides a better CE evaluation since it can model
119 every microphysical effect involved in the AP collection by cloud droplets (like Brownian motion,
120 inertial impaction, interception, etc.) and their coupling. Since the experiments have been
121 performed in a subsaturated air (relative humidity of 95.1 ± 0.2 %), we extend the Dépée et al. (2019)
122 model by adding the thermophoretic and diffusiophoretic effects. Finally, this study aims to
123 experimentally validate the Dépée et al. (2019) model to provide consistent theoretical CEs for a
124 convenient incorporation in cloud models, pollution models, climate models, and so forth.
125
126
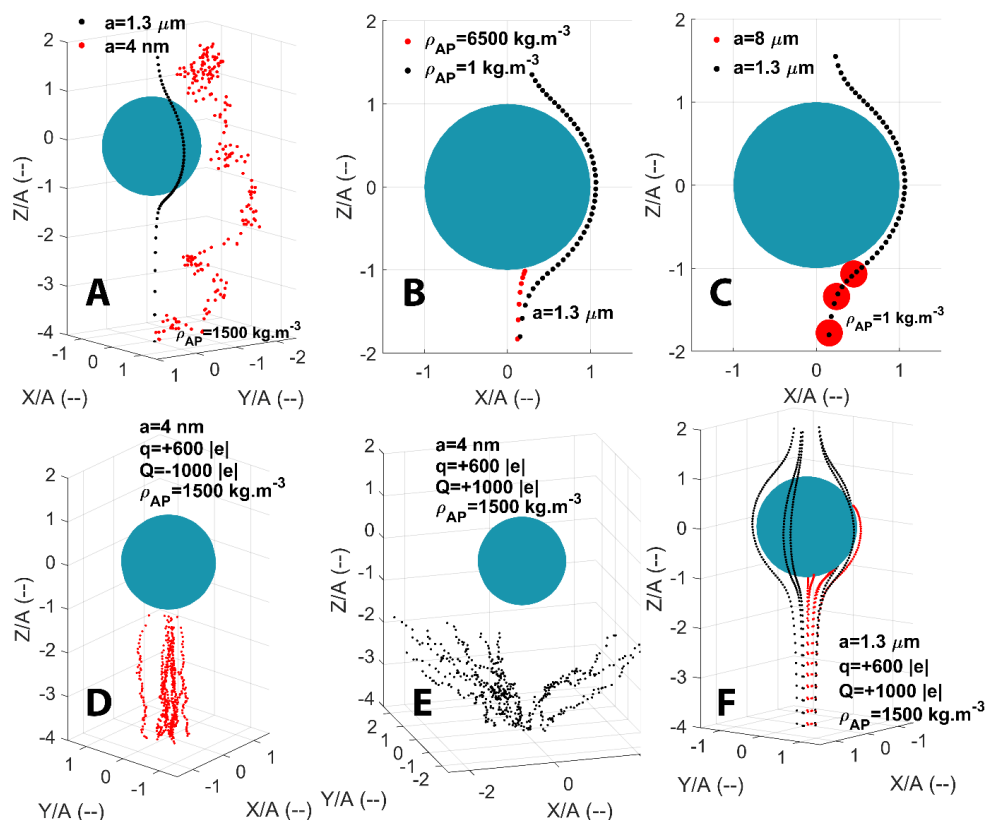
127
128 Figure 1 APs trajectories computed with the extended Dépée et al. (2019) model for a 50 µm droplet
129 radius (A) and AP with various radii (a) and densities (ρ_{AP}). The air temperature (T_{air}) and the air
130 pressure (P_{air}) are respectively -17°C and 540 hPa. From Figure 1 A to F, the considered effects are
131 the Brownian motion (A), the inertial impaction (B), the interception (C), the electrostatic forces
132 with attractive (D) and repulsive (E, F) Colomb forces. The droplet (Q) and AP (q) charges are
133 labelled. In Figures 1 B to F - the red trajectories result in an AP collection. Adapted from Part I
134 **(Dépée et al., 2020)**.
135
136

1   EXPERIMENTAL SETUP

1.1   Overview

Figure 2 shows the In-Cloud Aerosol Scavenging Experiment (In-CASE) which has been built to study the influence of the electric charges on the CE. Droplets fall at their terminal velocity into a chamber through an AP flow of 1.5 l/min. The In-CASE's chamber is subdivided into 3 parts - the injection head where droplets and APs are inserted; the collision chamber where droplets and APs interact with each other; the aerodynamic separator set at the bottom's chamber impacts droplets into an impaction cup while uncollected APs go out the chamber toward a High Efficiency Particulate Air (HEPA) filter. For this latter stage, an Argon updraft assures that there are no AP that settle into the droplet impaction cup. More details on the In-CASE's chamber can be found in **Dépée et al. (2020)**.

APs are atomised from a sodium fluorescein salt solution ($C_{20}H_{10}Na_2O_5$). This molecule has been used for its significant fluorescent properties, detectable at very low concentrations (down to 10^{-10} g/l). Once generated, the APs flow through a diffusion dryer and a portion of the flow is then directed into a Differential Mobility Analyser (DMA; TSI 3080) to select APs following their electrical mobilities whereas the overflow ends in an exhaust. At the DMA's outlet, the AP size distribution is assumed to be monodispersed (discussed in section 2.1). Thereafter, APs are electrically charged by a custom-designed field charger (section 1.4). Since the optimised AP flowrate in the charger is 1.5 l/min and the maximum AP flowrate in the DMA was 1.2 l/min during the experiments, a clean air flowrate is added at the charger's inlet. Before the AP injection in the In-CASE's chamber, the flow is humidified to assure a high relative humidity level inside the collision chamber (section 1.2). Before the AP collection on the HEPA filter, the APs flow through a low-energy X-ray neutraliser (< 9.5 keV, TSI 3088) to eliminate charge accumulation on this filter leading to AP deposition on the metallic walls of the filter holder.

Droplets are generated with a piezoelectric injector provided by Microfab (MJ-ABL-01 model) with an internal diameter of 150 µm - at 25 Hz to prevent droplets from coalescencing. The generator is set in a 3D printing which is located in the injection head (Figure 5, Right). An electrostatic inductor is also placed in the 3D printing to charge droplets (section 1.5). The droplet size is measured during experiments through two facing portholes in the injection head. Further details can be found in **Dépée et al. (2020)** but note that the size distributions of the droplets generated by the piezoelectric injector are considered monodispersed since the droplet size dispersion is very low ($\sigma\sim1\%$).

This In-CASE setup presented here is quite different from the other configuration regarding the relative humidity's influence developed in Part I **(Dépée et al., 2020)**.
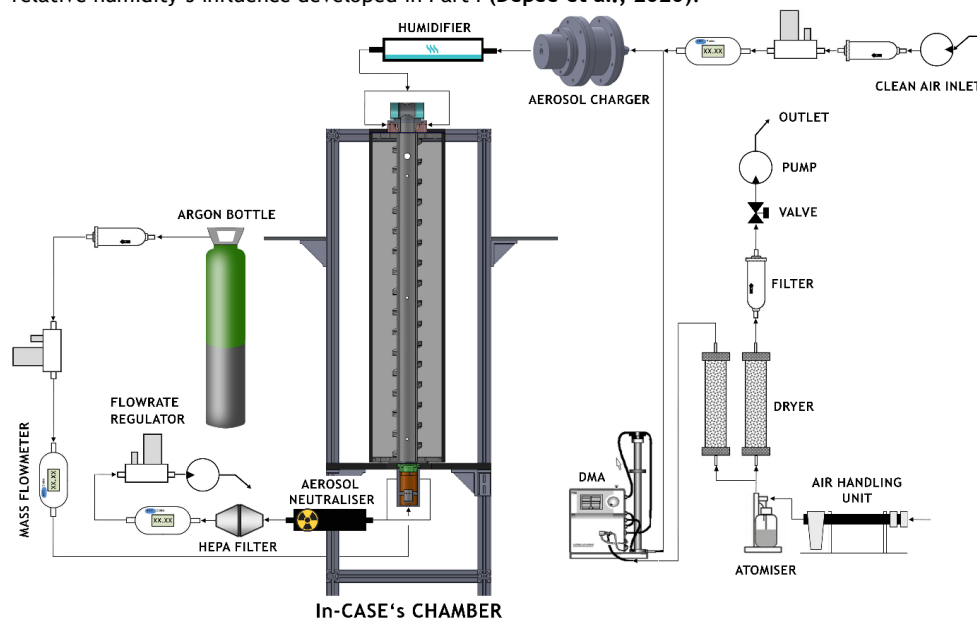
Figure 2 In-CASE setup to study the electric charges' influence - adapted from Part I **(Dépée et al., 2020)**.

1.2 Thermodynamic conditions in the In-CASE's chamber

Thermodynamic conditions were set as constant as possible during experiments to get comparable CE measurements. The pressure in the In-CASE's chamber was the atmospheric one and the global temperature for the campaign presented in this paper was $1.08 \pm 0.12 \,°C$. As referred in section 1.4 of **Dépée et al. (2020)**, the chamber's temperature is controlled through a cooling system which indirectly sets the relative humidity level in the chamber. Here, the temperature of the pure water in the humidifier placed before the In-CASE's chamber (Figure 2) was increased to get a global relative humidity level in the chamber of 95.1 ± 0.2 %. Note that this relative humidity level was the maximum which could be reached with In-CASE. So, the contribution of the thermophoretic and the diffusiophoretic effects in the CE measurements was reduced as much as possible.

1.3 Droplet evaporation

The droplet evaporation was theoretically evaluated similarly to subsection 1.4.2.2 of **Dépée et al. (2020)**. For a relative humidity level of 95 %, it was found that the droplet radius decreases by less than 0.5 % from the droplet generation to the bottom of the collision chamber. Thus, the evaporation in the In-CASE collision chamber was neglected for the discussions below.

1.4 AP charging

APs are electrically charged by passing through a custom-designed field charger adapted from Unger et al. (2004). The scaled geometry is presented in Figure 3. This charger is based on a system of electric discharges produced between a high potential tungsten wire and a grounded cylinder. A metallic converging portion is used at the charger's outlet to trap ions and assure only charged APs can leave the charger. A Teflon ball (Ø=1 mm) is set at the end of the tungsten wire to ensure there is no point effect between the wire and the ion trap. A large number of ions are then created and migrate between the two centimeters interelectrode space along the electric field lines. Finally, the APs flow through them and get charged by ion attachment.
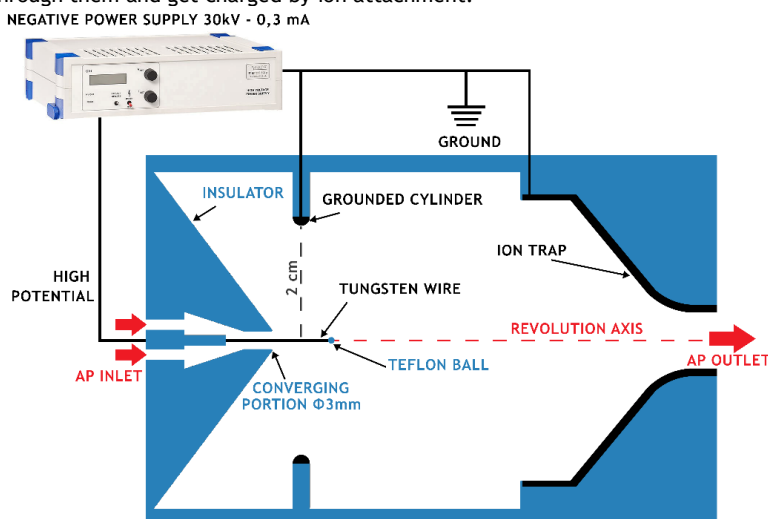
Figure 3 Geometry of the home-made AP charger based on Unger et al. (2004) (at scale).

The charging relationships of the charger used during all experiments are presented in Figure 4. They provide the mean electric AP charge related to the potential at the tungsten wire for the 4 AP radii considered here. It results from *ex situ* experiments which are detailed in Appendix A. Note that APs are negatively charged through the discharge regime used (negative Trichel regime) and there is an electric potential where the AP charge saturates which is typical for field chargers (Pauthenier and Moreau-Hanot, 1932). These results were performed at an AP flowrate of 1.5 l/min which was found to maximise the AP penetration inside the charger and consequently the AP concentration inside the In-CASE's chamber. Penetration tests - not presented in this study - were deduced by variating the AP flowrate in the setup detailed in Appendix A.
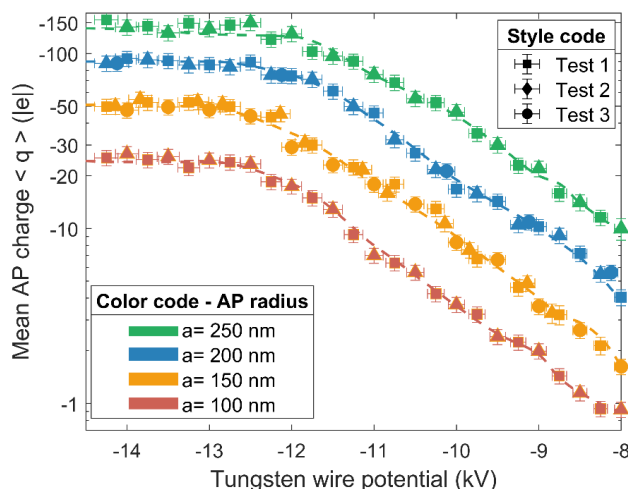
212
213
214 Figure 4 AP charging relationships used during experiments for the 4 AP radii (a) considered. Error
215 bars represent the standard deviations in measurements.
216

217 **1.5   Droplet charging**
218 The droplets charge is controlled through an electrostatic inductor adapted from Reischl et al. (1977).
219 Two parallel metallic plates are set at the droplet generator's nozzle (Figure 5, left) - one plate
220 connected to the neutral potential and the other one to a potential referred as V_{ind}. It induces an
221 electric field ($E_{ind} \sim 10^2$-10^3 V/m) at the nozzle. Since sodium chloride is added to the pure water that
222 feeds the piezoelectric droplet generator, this electric field can selectively attract negative or
223 positive ions toward the nozzle where the droplet is formed, according to its sign. If V_{ind} is negative,
224 the positive sodium ions (Na^+) migrate toward the nozzle and the negative chloride ions (Cl^-) are
225 repulsed from the nozzle and inversely if the potential is positive. Furthermore, the amplitude of the
226 electric field (E_{ind}) sets the ion quantity in the droplet. Note that the sodium chloride concentration
227 has no impact on the induced droplet charge if the ion number is large enough for the entire
228 experiment time (Reischl et al., 1977) - 3.3 g/l was used here.
229
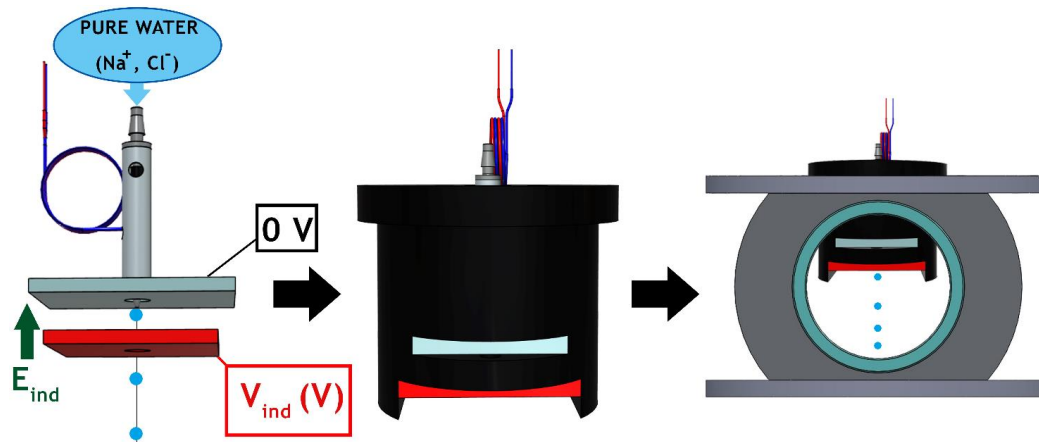
230
231
232 Figure 5 (**Left**) Electrostatic inductor below the piezoelectric droplet generator. (**Center**) 3D printing
233 containing droplet generator and electrostatic charger. (**Right**) Injection head at the top of the In-
234 CASE's chamber containing the 3D printing.
235

236 A method to evaluate the droplet charge was developed in this study and is detailed in Appendix B.
237 In Figure 6, the resulting charging relationship of the electrostatic inductor is presented. It gives the
238 droplet charge (Q) as a function of the electrostatic inductor potential (V_{ind}). We note that the
239 droplet generator produces highly electrically charged droplets since the droplet charge is evaluated
240 to about -8,400 elementary charges, for a zero potential at the inductor plate (V_{ind}= 0 V). This is in
241 line with Ardon-Dryer et al. (2015) which used a similar generator and measured up to 10^4 elementary
242 charges on the generated droplets. Finally, this charging relationship is used during experiments to
243 positively or negatively set the droplet charges. The electrostatic inductor and the droplet generator
244 are placed into a 3D printing (Figure 5, center), this latter being placed in the injection head at the
245 top of the In-CASE's chamber (Figure 5, right).
246
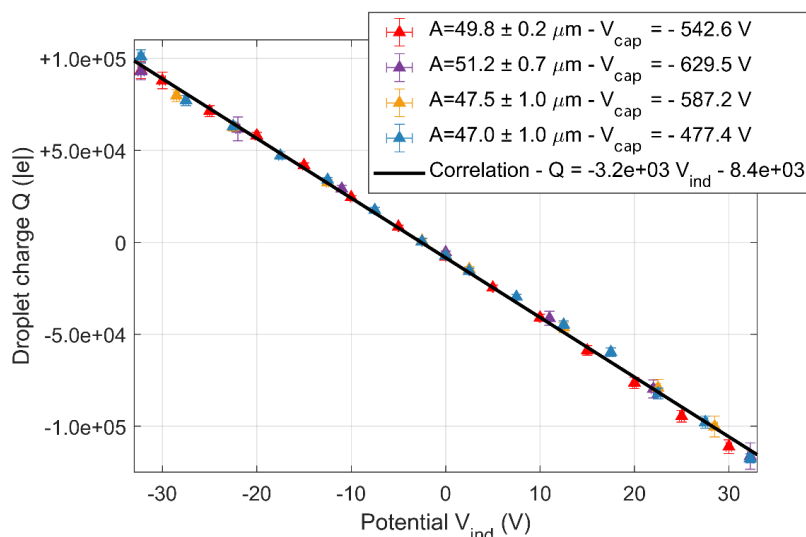
247
248
249 Figure 6 Charging low of the electrostatic inductor - colors identify different tests performed to
250 ensure there is no droplet charge modification over time and manipulations. Error bars represent the
251 standard deviation of the droplet radii evaluated. The parameter V_{cap} is the potential at the capacitor
252 to measure the droplet radius (see Appendix B).
253
254 **2   DATA ANALYSIS**
255
256 **2.1   Assumption of a monodispersed AP size distribution**
257
258 As a reminder, APs flow through a DMA (Figure 2) to select APs following their electrical mobility. As
259 explained in section 2.2 of the Part I (**Dépée et at., 2020**), several AP radii can actually be selected
260 depending on their elementary charges given that they have the same electrical mobility. For
261 example, with a selected AP radius of 100 nm at the DMA (considering one elementary charge on it),
262 the double charged AP radii of 161.8 nm will also be selected.
263
264 Sometimes, the multiple charged APs cannot be neglected in the AP flow at the DMA's outlet. The
265 CE deduction is then more difficult (**Dépée et al., 2020**). Here, the aerodynamic impactor at the
266 DMA's inlet as well as the AP flowrate in the DMA were optimised to prevent double (and more)
267 charged AP from being selected by the DMA. Indeed, the cut-off radius of the impactor at the DMA's
268 inlet (referred as $D_{50\%}/2$) - which is the radius where 50 % of the APs are impacted - is small enough
269 compared to the double charged AP radius. This is summarised in the Table 1 for all selected AP radii
270 used in the experiments. Thus, the AP size distribution at the DMA outlet is assumed to be
271 monodispersed and the CE is deduced as follows.
272
273

274   Table 1 AP selection parameters

Selected AP radius by the DMA (single charged)	Double charged AP radius with the same electrical mobility	AP flowrate in the DMA	Cut-off radius of the impactor at the DMA inlet ($D_{50\%}/2$)
100 nm	161.8 nm	1.2 l/min	140 nm
150 nm	253.7 nm	1.0 l/min	157 nm
200 nm	348.3 nm	0.6 l/min	213 nm
250 nm	444.3 nm	0.4 l/min	268.5 nm

275
276
277 **2.2 Collection efficiency definition**
278
279 The collection efficiency (CE) is calculated from the equation (1):

$$CE(a, A, q, Q, HR) = \frac{m_{AP,d}}{m_{AP,available}} \qquad (1)$$

280 Where $m_{AP,d}$ is the AP mass collected by all droplets which is directly measured by fluorescence
281 spectrometry analysis of the droplets collected in the impaction cup, which is located at the bottom
282 of the In-CASE chamber (Figure 9 of **Dépée et al., 2020**). $m_{AP,available}$ is the mass of available APs in
283 the volume swept by all droplets - evaluated with the equation (2) :

$$m_{AP,available} = \pi(A + GroF(RH) \times a)^2 \times F_d \times \Delta t \times H_{eff} \times C_{m,AP} \qquad (2)$$

284 With F_d - the droplet generation frequency, Δt - the experiment duration (on average 4 hours and a
285 half in this campaign), a - the AP dry radius, $GroF$ - the growth factor depending on the relative
286 humidity (RH). This latter characterises the hygroscopicity of the sodium fluorescein salt - further
287 details related to its evaluation can be found in section 1.4.2 of **Dépée et al. (2020)**. H_{eff} is the
288 effective height of interaction between APs and droplets calculated with the equation (3):

$$H_{eff} = \frac{U_{A,\infty}}{U_{A,\infty} + V_Q} H_{In-CASE} \qquad (3)$$

289 With the AP flow velocity (V_Q) equal to 1.3 cm/s (for an AP flowrate of 1.5 l/min), the droplet
290 terminal velocity ($U_{A,\infty}$) assumed to be equal to 25 cm/s and the In-CASE collision chamber's height
291 ($H_{In-CASE}$) of 1 meter.
292
293 In equation (2), the mean AP mass concentration ($C_{m,AP}$) in the In-CASE collision chamber is evaluated
294 from the fluorescence spectrometry analysis of the HEPA filter. It is given by the equation (4) where
295 $Q_{In-CASE,c}$ is the AP flowrate going through the In-CASE collision chamber.
296

$$C_{m,AP} = \frac{m_{AP,tot}}{\Delta t \times Q_{In-CASE,c}} \qquad (4)$$

297
298 **2.3 Uncertainties**
299
300 Uncertainties are not detailed in this paper but were addressed in Part I, section 2.3 (**Dépée et al.,**
301 **2020**).
302
303
304
305

3   RESULTS AND DISCUSSIONS

3.1   Extension of the Dépée et al. (2019) model

CE measurements are compared to the model of Dépée et al. (2019) which models the electrostatic forces (F_{elec}) between droplets and APs in the CE calculation. Since the global relative humidity level was 95.1 ± 0.2 % in all experiments, the thermophoretic (F_{th}) and the diffusiophoretic (F_{df}) forces were also considered to get the theoretical CE values. Indeed, **Dépée et al. (2020)** showed that the contribution of these two effects for a comparable relative humidity level is significant. Thus, the Dépée et al. (2019) model is extended here by replacing the resulting velocity at the AP location ($\boldsymbol{U}_{f@p}{}^{*}$ in their Equation 6) by the new equation (5):

$$\boldsymbol{U}_{f@AP}{}^{*}(t) = \boldsymbol{U}_{f@AP}(t) + \frac{\tau_p}{m_p}\big(\boldsymbol{F_{buoy}} + \boldsymbol{F_{df}} + \boldsymbol{F_{elec}} + \boldsymbol{F_{th}}\big) \tag{5}$$

Where the analytical expressions of F_{buoy} is detailed in equation system (9), F_{df} and F_{th} in **Dépée et al. (2020)** - equations (12) - and F_{elec} is defined in equation (7) :

$$\boldsymbol{F_{elec}} = \frac{q^2}{4\pi\varepsilon_0 A^2}\left[\overbrace{\left(-\frac{r^*}{(r^{*2}-1)^2}+\frac{1}{r^{*3}}\right)}^{Short-range\ attractive\ term} + \underbrace{\frac{1}{r^{*2}}\times\frac{Q}{q}}_{Coulomb\ inverse\ square\ term}\right]\boldsymbol{u_r} \tag{6}$$

With ε_0 - the permittivity of the free space, $\boldsymbol{u_r}$ - the unit vector in the radial direction from the droplet centre to the AP centre, r^* - the distance between the AP and droplet centres, normalised by the droplet radius A.

3.2   Collection efficiency measurements

The CE measurements for various charges are presented in Table 2 for the 4 AP wet radii (a_{wet}) considered in this study. The droplet (Q) and AP (q) charges are also informed by number of elementary charges. The global temperature was 1.08 ± 0.12°C for a global relative humidity level of 95.1 ± 0.2 % and a droplet radius of 48.5 ± 1.1 μm. Note that the wet AP density depends on the one of sodium fluorescein salt and water. Equation (1) of **Dépée et al. (2020)** yielded a density of about 1116 kg.m^{-3}.

Table 2 CE measurements

a_{wet} (nm) / q (|e|)	$Q(|e|)$ 9.6 × 10⁴ ± 4.3 × 10³	3.0 × 10⁴ ± 1.9 × 10³	5.0 × 10³ ± 8.4 × 10²	0 ± 6.0 × 10²	−5.0 × 10³ ± 7.7 × 10²	−1.0 × 10⁴ ± 8.7 × 10²	−3.0 × 10⁴ ± 1.4 × 10³
175 ± 3 : −10 ± 1	3.91×10^{-2}	2.44×10^{-2}	3.47×10^{-3}	4.17×10^{-3}	5.58×10^{-3}	9.81×10^{-4}	2.55×10^{-4}
175 ± 3 : −20 ± 2	6.77×10^{-2}	3.47×10^{-2}	6.99×10^{-3}	5.07×10^{-3}	4.25×10^{-3}	9.17×10^{-4}	4.12×10^{-5}
260 ± 3 : −11 ± 1	2.41×10^{-2}	1.30×10^{-2}	3.25×10^{-3}	2.97×10^{-3}	2.14×10^{-3}	1.34×10^{-3}	1.93×10^{-4}
260 ± 3 : −30 ± 3	7.91×10^{-2}	2.31×10^{-2}	7.96×10^{-3}	5.75×10^{-3}	3.47×10^{-3}	2.57×10^{-3}	4.97×10^{-5}
346 ± 4 : −10 ± 1	2.24×10^{-2}	8.98×10^{-3}	3.03×10^{-3}	1.86×10^{-3}	1.84×10^{-3}	1.05×10^{-3}	5.20×10^{-4}
346 ± 4 : −34 ± 3	4.58×10^{-2}	1.40×10^{-2}	5.39×10^{-3}	3.91×10^{-3}	2.90×10^{-3}	2.23×10^{-3}	3.60×10^{-5}
346 ± 4 : −71 ± 7	9.17×10^{-2}	3.25×10^{-2}	1.70×10^{-2}	7.33×10^{-3}	5.51×10^{-3}	2.88×10^{-3}	2.21×10^{-5}
432 ± 5 : −22 ± 2	3.74×10^{-2}	1.49×10^{-2}	3.22×10^{-3}	2.49×10^{-3}	1.85×10^{-3}	2.44×10^{-3}	1.25×10^{-4}
432 ± 5 : −52 ± 5	7.62×10^{-2}	4.13×10^{-2}	1.13×10^{-2}	3.23×10^{-3}	3.23×10^{-3}	4.17×10^{-3}	1.06×10^{-4}
432 ± 5 : −90 ± 9	1.77×10^{-1}	3.55×10^{-2}	1.83×10^{-2}	6.90×10^{-3}	4.75×10^{-3}	4.56×10^{-3}	2.43×10^{-5}

333
334   3.2.1   Effect of the product of the droplet and AP charges on the collection efficiency

335
336   The CE measurements for a wet AP radius of 432 nm are presented in Figure 7 as a function of the
337   product of the droplet (Q) and AP (q) charges. An important charge influence is measured, increasing
338   or decreasing the CE up to two orders of magnitude for large negative or positive charge products,
339   respectively, compared to the theoretical CE value disregarding the electrostatic effects (dashed line
340   in Figure 7). This is due to the Coulomb inverse square term in the electrostatic forces' equation (6)
341   which dominates - attracting or repulsing the APs from the droplet depending on the fact that AP and
342   droplet charges have unlike or like signs.
343   For small positive charge products (approximately $q \times Q \leq 10^6 \, |e| \times |e|$), an increase of CE with a
344   factor of more than three is measured compared to the theoretical CE value without electrostatic
345   forces. This fact truly emphasises the contribution of the short-range attractive term in equation (6)
346   which attracts the APs toward the droplet even though the droplet and AP charges have like signs.
347   Indeed, as previously stated, this term prevails for small charge products (Dépée et al., 2019).

348
349   Note that the same observations can be made for the other wet AP radii, with a measured influence
350   of the electric charges on CE up to four orders of magnitude.
351
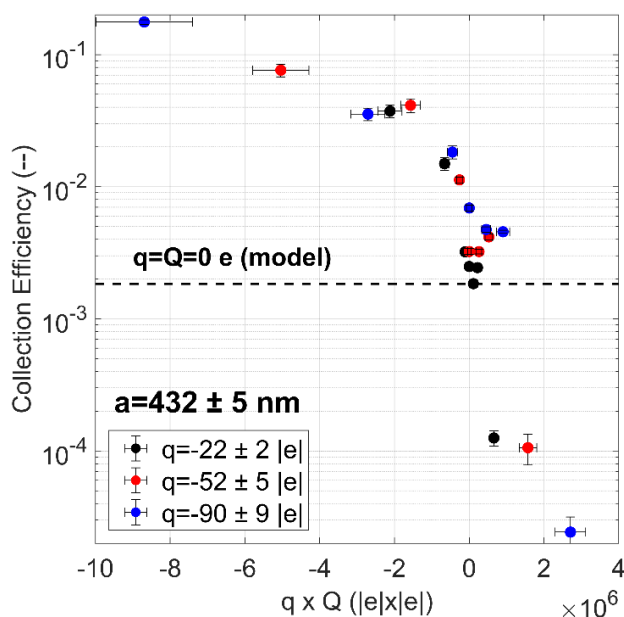
352
353   Figure 7 CE measurement as a function of the product of the droplet (Q) and AP (q) charges for the
354   wet AP radius of 432 nm. Color code informs about the AP charge. The dashed line represents the
355   theoretical CE value disregarding the electrostatic forces (given the air parameters 1°C, 1 atm, 95%
356   of relative humidity).

357
358
359
360   3.2.2   Effect of the AP charge on the collection efficiency for a neutral droplet

361
362   In Figure 8, the CE measurements for a neutral droplet are presented for the 4 wet AP radii - referred
363   by the color code - with the respective theoretical CE values without electrostatic forces (the dashed
364   lines).
365   Note that the contribution of the electrostatic forces seems insignificant for an AP charge of about
366   -10 elementary charges and an AP radius of 346 nm and 260 nm as well as an AP of 432 nm with -20
367   elementary charges. Indeed, these measurements are very close to the theoretical ones with no
368   consideration of electrostatic forces. Several microphysical effects have probably an equivalent

369 contribution on the CE measurements such as electrostatic, thermophoretic and diffusiophoretic
370 forces, in addition to AP diffusion, weight and inertia.
371 Nevertheless, for the 4 AP radii, an increase of the CE considering more elementary charges on the
372 APs is measured - even though the droplet is neutral (or within uncertainties weakly charged). For
373 example, given an AP radius of 346 nm, the CE is multiplied by almost a factor 4 when the AP charge
374 increases from -10 to -71 elementary charges. It highlights the contribution of the short-range
375 attractive term in equation (6), showing the presence of a surface charge distribution on the droplet
376 formed by the partial influence of the AP electrostatic field on it. In the current case, this is the only
377 contribution since the droplet is neutral and the Coulomb inverse square term is zero in equation (6).
378 This is an important result since to our knowledge, there is no experimental observation of the short-
379 range attractive term on the CE in the previous studies of the literature.
380 For a given AP charge, an increase of the CE is measured when the AP radius decreases, probably due
381 to the increase of the electrical mobility of APs. This is in line with the numerical results of Dépée
382 et al. (2019) even though electrostatic effects are not the only contribution involved in this CE
383 inscrease. Indeed, the Brownian motion of the APs increases for smaller APs and enhances the
384 collision between the droplet and APs.
385 Moreover, the curve slope could be increased for a decrease of the AP radius since the electrical
386 mobility increases - but this tend is not visible in Figure 8. It can be due the uncertainties on the CE
387 measurements, the droplet neutralisation and the AP charge.
388
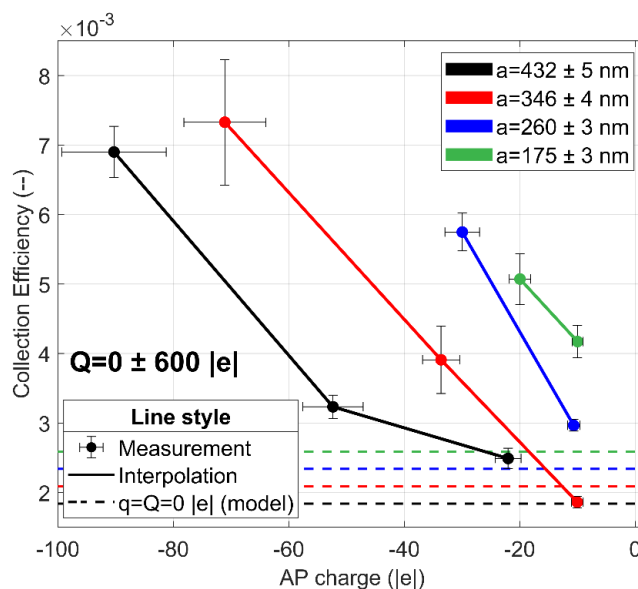
389
390 Figure 8 CE measurement as a function of the AP charge (q) for the 4 wet AP radii (Color code). The
391 droplet is neutral. The dashed line represents the theoretical CE value disregarding the electrostatic
392 forces (given the air parameters 1°C, 1 atm, 95% of relative humidity).
393
394
395
396
397 3.2.3   Comparison with existing models
398 In the next subsections, the CE measurements are confronted to two different models in order to
399 evaluate their robustness and the modelling of the observed effects.
400
401 3.2.3.1 Kraemer and Johnstone (1955) model
402 To describe the impact of the electric charges on the CE, there is the well-know correlation of
403 Kraemer and Johnstone (1955), summarised in equation (7):

$$EC_{KJ} = \left(\frac{Q}{\pi\varepsilon_0 A^2 \Delta U}\right)\left(\frac{q \times C_u}{6\pi\eta_{air}a}\right) \tag{7}$$

404 With η_{air} - the dynamic viscosity of air, C_u - is the Stokes-Cunningham slip correction factor (defined
405 in Appendix A of Dépée et al. (2019)) and ΔU the droplet fall velocity relative to the AP fall velocity.
406 This latter is assumed to be equal to $|U_{A,\infty} - U_{a,\infty}|$ where $U_{a,\infty}$ is the AP settling velocity.
407
408 Since this correlation models the contribution of the attractive Coulomb forces on the CE, only the
409 CE measurements with a negative charge product are compared. In Figure 9, the parity plot of the
410 modelled CE from the correlation of Kraemer and Johnstone (1955) as a function of the measured CE
411 is presented. The horizontal error bars are the measurement uncertainties while the vertical ones
412 are the extreme theoretical CE values considering the extreme droplet and AP charges (by adding or
413 subtracting the charge uncertainties). It is shown that the correlation of Kramer and Johnstone (1955)
414 accurately describes the observation for the large charge products (red color) but the discrepancies
415 between model and measurement increase when the charge product decreased (when color goes to
416 blue). Indeed, the less AP and droplet are electrically charged, the more the model underestimates
417 the CE compared to the observations. This is due to the formula which only models the attractive
418 Coulomb forces and disregards the other effects like the AP weight, the AP inertia and the AP diffusion
419 which tend to increase the CE as well as the diffusiophoretic and the thermophoretic forces (**Dépée**
420 **et al., 2020**). Consequently, the correlation gives better agreement for large charge products where
421 the attractive Coulomb forces dominate the other effects on the AP collection. This case illustrates
422 the strong interest of using Lagrangian models like the one of Dépée et al. (2019) which considers all
423 microphysical effects involved in the in-cloud AP collection and especially their coupling.
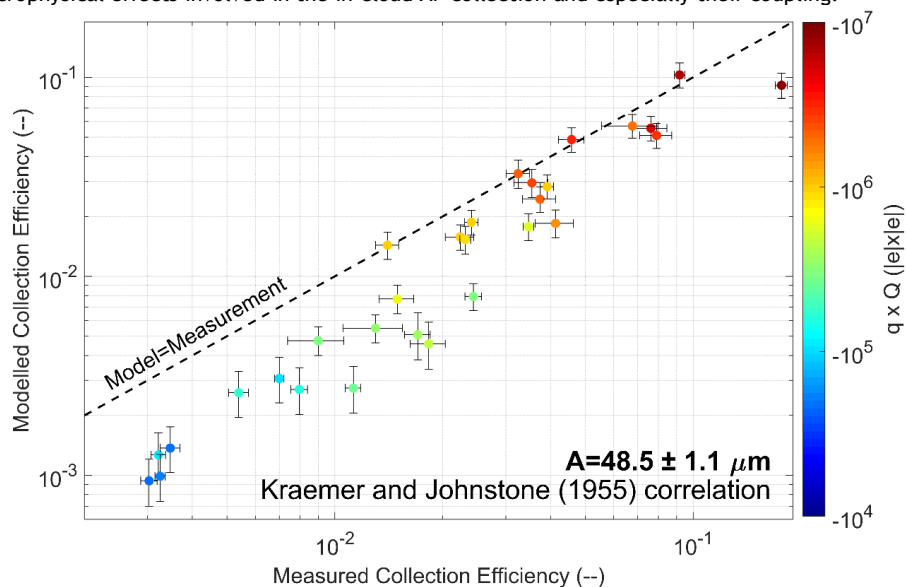
424
425 Figure 9 Parity plot - Modelled CE from the correlation of Kraemer and Johnstone (1955) as a function
426 of the measured CE. Only the negative charge products are considered here, represented by the color
427 code.
428
429 Note that Wang et al. (1983) also compared their CE measurements with this correlation, finding
430 good agreement since they considered between -10^7 and -10^8 elementary charges on droplets and
431 between 1 and 13.5 elementary charges on APs. So, their charge products were larger than the ones
432 used in the present study and they had no combined effect - the attractive Coulomb force was by far
433 the only significant contribution. It can explain why their comparison with the correlation of Kraemer
434 and Johnstone (1955) are better than the ones presented in Figure 9. Since most of the measurements
435 of Wang et al. (1983) are for a droplet radius of 250 μm, they are not compared to the present ones
436 which are significantly much smaller (A= 48.5 ± 1.1 μm).

437
438 3.2.3.2 Dépée et al. (2019) extended model
439 In Figure 10, the parity plot of the modelled CE from the extended model of Dépée et al. (2019) as a
440 function of the measured CE is presented. The modelled CE are calculated from the experimental
441 parameters (AP density, air temperature, pressure and relative humidity as well as the sizes and
442 charges) and the CE values less than 10^{-5} are set to 10^{-5} to avoid an excessive computation time
443 (Dépée et al., 2019). The horizontal error bars are the measurement uncertainties while the vertical
444 ones are the extreme theoretical CE values considering the extreme droplet and AP charges (by
445 adding or subtracting the charge uncertainties). The color code corresponds to the different droplet
446 radii studied.
447 It appears that there are as many data points above the parity curve as below, meaning that the
448 model overestimates as much as underestimates the observations. Thus, it can be assumed that there
449 is no missing or unnecessary microphysics effects in the CE modelling. Moreover, the mean difference
450 between the modelled CEs and the 70 measured CEs is 66 %. This is a reasonable value for a
451 microphysics parameter such as the collection efficiency which varies several orders of magnitude,
452 especially since the value was calculated disregarding the different uncertainties (error bars in
453 Figure 10) and was as a result over-evaluated.
454 Nevertheless, 6 data points seem inconsistent with discrepancies between model and measurements
455 from 150 to 1000 %, occurring for the smallest CE values in Figure 10 (lower left). Note that the
456 discrepancies should be even worse since the modelled CEs, set to 10^{-5}, are actually much lower. By
457 examining these data points, it appears that the measured AP masses in the droplet impaction cup -
458 $m_{AP,d}$ in equation (1) - are very close to the detection limit of the spectrometer used. Moreover, for
459 the experimental conditions, the model predicts AP masses in the droplets lower than the detection
460 limit since the Coulomb inverse square term in equation (6) was very repulsive. So, the assumption
461 can be made that a pollution occurred during the various steps of the protocol (end of experiment,
462 disassembly of the chamber's bottom to reach the droplet impaction cup, change of room for the
463 analysis, etc.). Note that the detection limit of the spectrometer is 10^{-15} kg (for the nominal analysis
464 volume considered) which only represents ten APs with a dry radius of 250 nm deposited on the
465 droplet impaction cup. Thus, it exists an important uncertainty in these CE measurements related to
466 a possible contamination which is difficult to quantify. To reduce it, it would be necessary to work
467 in a cleanroom or increase the experiment duration to avoid detection problem. However, for these
468 data points the experiment duration was almost 6 hours (without mentioning the preparation, the
469 purging and the cleaning durations) and, beyond this duration, stability problems of the piezoelectric
470 droplet generator were frequent.
471
472 However, a reasonable agreement between the extended model of Dépée et al. (2019) and the CE
473 measurements are observed. As a reminder, the mean discrepancy was over-evaluated at 66 % which
474 is suitable to describe a microphysical parameter varying on several orders of magnitude for the
475 collection efficiency. Furthermore, if the 6 inconsistent values are removed - the mean discrepancy
476 on the 63 remaining CE measurements decreases from 66 to 38 %.
477
478 The 38 % of discrepancy between the Dépée et al. (2019) extended model and the measurements can
479 be attributed to the dispersion of the AP charge distribution. Indeed, it was not possible to
480 characterize the AP charge distribution which remains an important uncertainty. Moreover, the AP
481 size distribution was assumed to be monodispersed but a dispersion exists, even if very small, which
482 depends on the spectral bandwidth of the DMA. This one can induce some larger (or smaller) APs
483 inside the AP charger which can get an electric charge significantly larger (or smaller) than the
484 predicted one since the charging process is roughly proportional to the AP surface. Then, in the In-
485 CASE chamber, some larger (or smaller) APs with a larger (or smaller) electric charge can interact
486 with the droplets and notably change the final AP mass collected by the droplets during an
487 experiment ($m_{AP,d}$). Another possible explanation is the differences in temperature and relative
488 humidity between the top and the bottom chamber, respectively less than 1 °C and 4 % (addressed in
489 **Dépée et al. (2020)**). It could induce local discrepancies during the AP travel time in the chamber in
490 term of AP density (through the hygroscopicity) or thermophoretic and diffusiophoretic forces which
491 can change the likelihood of being collected by the droplets and then slightly change $m_{AP,d}$. See
492 **Dépée et al. (2020)** for a discussion of the influence of these two latter forces on the CE.
493
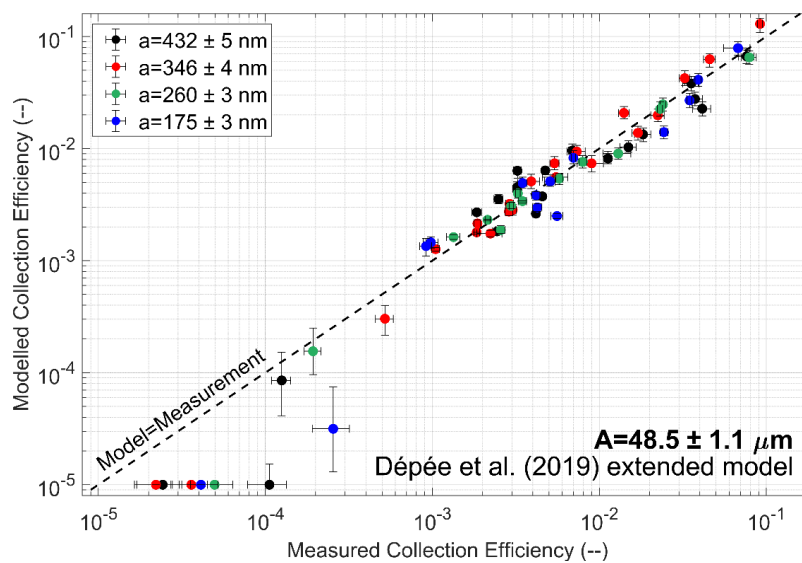
494
495 Figure 10 Parity plot - Modelled CE from the extended model of Dépée et al. (2019) as a function of
496 the measured CE. The color code referrers to the droplet radius.
497

CONCLUSION

499 In-CASE (In-Cloud Aerosol Scavenging Experiment) was developed to conduct a series of experiments
500 evaluating the contribution of microphysical effects on the AP collection by falling cloud droplets.
501 For this purpose, all the parameters influencing the collection efficiency (CE) are controlled - i.e.
502 the AP and droplet sizes, the AP and droplet electric charges and the relative humidity. A first
503 campaign was performed to study the influence of the relative humidity which is the topic of the
504 Part I (**Dépée et al., 2020**). This current study was dedicated to a second topic - aiming the impact
505 of the electric charge on the CE. Furthermore, the CE measurements allow to validate existing models
506 like the Lagrangian one of Dépée et al. (2019) which considers all microphysical effects involved in
507 the AP collection by cloud droplets. Indeed, the literature lacks baseline data to get a suitable
508 comparison with the modelling since most of the previous studies failed to control all parameters
509 influencing the CE like the AP and droplet sizes and charges as well as the relative humidity (Beard,
510 1974 ; Lai et al., 1978 ; Barlow and Latham, 1983 ; Byrne and Jennings, 1993). Even though some
511 studies stand out (Wang and Pruppacher, 1977 ; Wang et al., 1983), no one examined the influence
512 of the electrostatic forces when the droplet and AP charges had like signs. Thus, the short-range
513 attractive term from the analytical expression of the electrostatic forces - equation (6) - used in the
514 current Lagrangian models (Tinsley and Zhou, 2015 ; Dépée et al., 2019) has never been
515 experimentally validated or at least emphasised.
516 In the new measured CE dataset, the APs and droplets are accurately charged through custom-made
517 droplet and AP chargers detailed above. Since both charge polarities are found in clouds (Takahashi,
518 1973), the droplets were negatively as well as positively charged during experiments. Moreover,
519 several amounts of elementary charges on the droplet were considered to represent a neutral droplet
520 but also the weakly and strongly charged droplets respectively found in stratiform and convective
521 clouds (Takahashi, 1973). The AP charge varied from the neutralisation to -90 ± 9 elementary charges
522 depending on the AP size to represent different charges encountered in the atmosphere, particularly
523 the ones of radioactive APs. Note that radioactive APs are known to get positively charged (Clement
524 and Harrison, 1992) whereas the APs were negatively charge in this work, through the charging regime
525 used in the AP charger (for integrity of the tungsten wire over time). Nevertheless, since we got the
526 relation $\boldsymbol{F}_{elec}(q, -Q) = \boldsymbol{F}_{elec}(-q, Q)$ in equation (6), the CE measurements with the same $\frac{q}{Q}$ ratios are
527 equivalent, assuming this analytical expression is validated by the measurements. The
528 thermophoretic and diffusiophoretic effects were reduced as mush as possible by maximising the

529 relative humidity during experiments at 95.1 ± 0.2 %. Since **Dépée et al. (2020)** measured a
530 contribution for a comparable relative humidity level, these two forces were added to the Dépée and
531 al. (2019) model. Finally, 4 radii of moist AP were used from 175 ± 3 to 432 ± 5 nm for one droplet
532 radius of 48.5 ± 1.1 µm.
533 From the 70 measurements obtained, an influence of the electric charges of 4 orders of magnitude
534 on the CE was observed, strongly increasing or decreasing the CE for large charge products,
535 respectively negative or positive. An increase of the CE was also measured by considering more
536 elementary charges on the APs even though the droplets were neutral (within uncertainties). This
537 observation is an important result since it emphasises the contribution of the short-range attractive
538 term in the electrostatic forces (equation (6)). It validates a surface charge distribution on the
539 droplet, formed by the partial influence of the AP electric field on it, which has never been
540 experimentally shown, to our knowledge, in the literature before.
541 The CE measurements with opposite signs on the droplet and AP were compared to the correlation
542 of Kraemer and Johnstone (1955), giving good agreements for large negative charge products where
543 the Coulomb attractive forces prevail over the other dynamic effects. This is in line with the work of
544 Wang et al. (1983) who also obtained good agreements, considering another droplet radius (250 µm)
545 and larger negative charge products. However, in the present study, an increase of the discrepancies
546 between the correlation and the measurement was measured when reducing the number of
547 elementary charges. This is due to the electrostatic forces not being the only effect involved in the
548 AP collection. There is actually a coupling of electrostatic, diffusiophoretic and thermophoretic
549 forces as well as the AP diffusion, weight and inertia. Thus, when the charge product is not strong
550 enough (gets significantly smaller than 10^7 $|e|\times|e|$), Lagrangian models as the one of Dépée et al.
551 (2019) remain the best estimation of the CE.
552 Finally, the CE measurements were also compared to the extended model of Dépée et al. (2019),
553 showing a really good description of the observed effects. Indeed, the mean discrepancy of the
554 modelling and the 70 measurements was 66 % which is suitable for a microphysical effect varying on
555 several orders of magnitude like the collection efficiency. This value was even better when 6
556 inconsistent measurements, probably contaminated, were disregarded – as it decreases from 66 % to
557 38 %. Moreover, note that the model overestimates as much as underestimates the observations so
558 that the discrepancies probably result from remaining uncertainties (like the dispersion of the AP
559 charge distribution) instead of a missing microphysical effect in the CE modelling.
560 To conclude, 70 new CE measurements are now available considering the influence of the electric
561 charges, showing significant differences with the previous CE measurements and theoretical values
562 from the literature which disregard the electrostatic forces. Thus, it appears to be essential to study
563 the impact of the new baseline data in a cloud-model like DESCAM (Detailed SCAvenging Model,
564 Flossmann, 1985) to examine the influence of the electric charges on the total wet AP removal in the
565 atmosphere. It could strongly affect the atmospheric AP removal since cloud droplets are known to
566 be charged (Takahashi, 1973) as well as the atmospheric AP, even more when APs are radioactive.
567 Indeed, Dépée et al. (2019) estimates that the electric charge of the radioactive APs emitted after
568 the Fukushima accident in 2011 was up to 600 elementary charges. Thus, AP removal could be
569 substantially affected by the electrostatic forces in-cloud and significantly change the ground
570 contamination after a discharge of radioactive materials from a nuclear accident. Since the new
571 Lagrangian model of Dépée et al. (2019) showed an accurate description of the influence of the
572 electric charges (and also of the relative humidity, studied in Part I **(Dépée et al. (2020))** on the CE,
573 this latter constitutes a simple, convenient and rapid manner to obtain a CE evaluation for its
574 incorporation in cloud models.
575
576
577
578
579

580 **Appendix A - AP charger**

581 **A.1 AP charging relationship's acquisition**
582 The AP charging relationships were obtained by performing *ex situ* experiments with the setup
583 presented in Figure 11. A nominal AP flow goes through the charger with a monodispersed AP size
584 distribution. At the charger's outlet, the flow of charged AP is subdivided - 0.6 l/min is directed to a
585 Condensation Particle Counter (CPC; TSI 3787) to deduce the concentration number of AP in the
586 charger ($C_{N,AP}$) while the other part goes toward an electrometer to measure the current (I_{elect}) due
587 to the charge evacuation. Before entering the CPC, APs are neutralised to avoid any deposition on
588 the metallic walls of the CPC and then the AP flow passes through a diffusion battery to filter the
589 fine particles produced during the discharges inside the charger. The mean AP charge ($\langle q \rangle$) was then
590 calculated from the equation (8) with the elementary charge (e) and the AP flowrate in the
591 electrometer (Q_{elect}):

$$\langle q \rangle = \frac{I_{elect}}{e \times C_{N,AP} \times Q_{elect}}$$
(8)

592 Several AP flowrates in the charger ($Q_{charger}$) were considered to study the AP penetration. When
593 $Q_{charger}$ was less than 0.7 l/min, clean air was added before the CPC to maintain a CPC flowrate of
594 0.6 l/min - this part is presented in the red dashed rectangle in Figure 11. From these experiments,
595 it was found that $Q_{charger}$=1.5 l/min maximises the AP penetration through the charger.
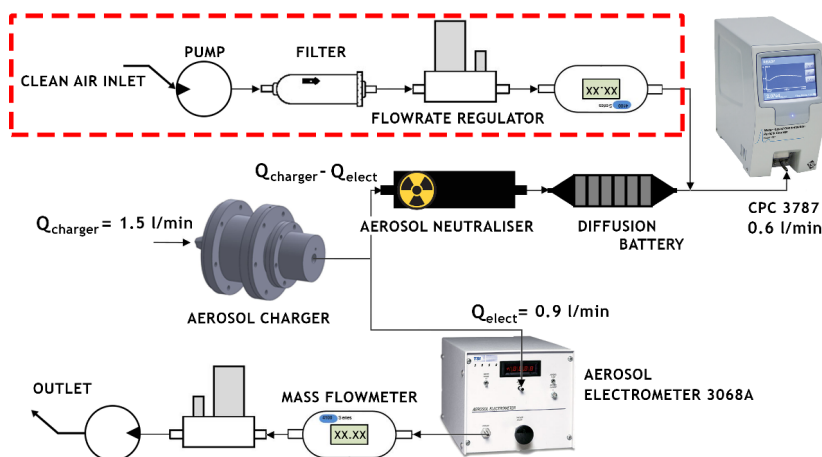
596

597 Figure 11 Setup to obtain the AP charging relationship. The red dashed rectangle is the part added
598 to study the AP penetration through the charger.
599

600 **A.2 Validation**
601 The setup (Figure 11) was conducted with the charger turned off to measure the mean AP charge
602 after the DMA. It was found one elementary charge on APs which validates that the multiple charged
603 APs are stopped at the DMA's inlet by the aerodynamic impactor. Thus, the assumption made that
604 the AP size distribution is monodispersed after the DMA is justified. The AP charge was also analysed
605 during 5 hours - no AP charge modification was measured over time. Moreover, the saturated AP
606 charges visible in Figure 4 for a tungsten wire potential less than -12.5 kV was also compared to the
607 theoretical values of Pauthenier and Moreau-Hanot (1932) - giving a good agreement.

608 Note that two other characterizations were made during these *ex situ* experiments like the
609 determination of the ion current between the grounded cylinder and the tungsten wire (Figure 3) or
610 the discharge frequencies - these both parameters are related to the tungsten wire potential. These
611 curves were used to precisely identify the discharge regime of the charger (Unger, 2001) - the
612 negative Trichel regime which provides a large discharge frequency and then a spatially homogeneous
613 particle charging around the tungsten wires.

614 **Appendix B - Droplet charging relationship obtention**

615 **B.1   Overview**
616 The Figure 12 presents the setup used in *ex situ* experiments to measure the droplet charge where
617 the charging relationship in Figure 6 comes from. The 3D printing - containing the droplet injector
618 and the charging system (detailed in section 1.5) - is set above a capacitor composed of one neutral
619 potential plate and another plate connected to a high potential (V_{cap}). In this latter, pictures are
620 obtained by optical shadowgraphy to get the droplet trajectories. The electric field (E_{cap}) induced
621 in the capacitor disturbs the droplet motion according to its electric charge. Thus, the droplet charge
622 is evaluated by finding the one which fits the best the theoretical droplet trajectory - deduced from
623 the 2nd Newton's law - and the measured droplet trajectories. A Faraday cage ensures the electric
624 field at the capacitor (E_{cap}) has no effect on the electric field at the electrostatic inductor (E_{ind}).
625 Since this is not a proper Faraday cage because of the holes for droplets and camera, a horizontal
626 metallic perforated plate is added below the 3D printing and connected to the neutral potential to
627 prevent the electric field (E_{cap}) from changing the droplet charge.
628
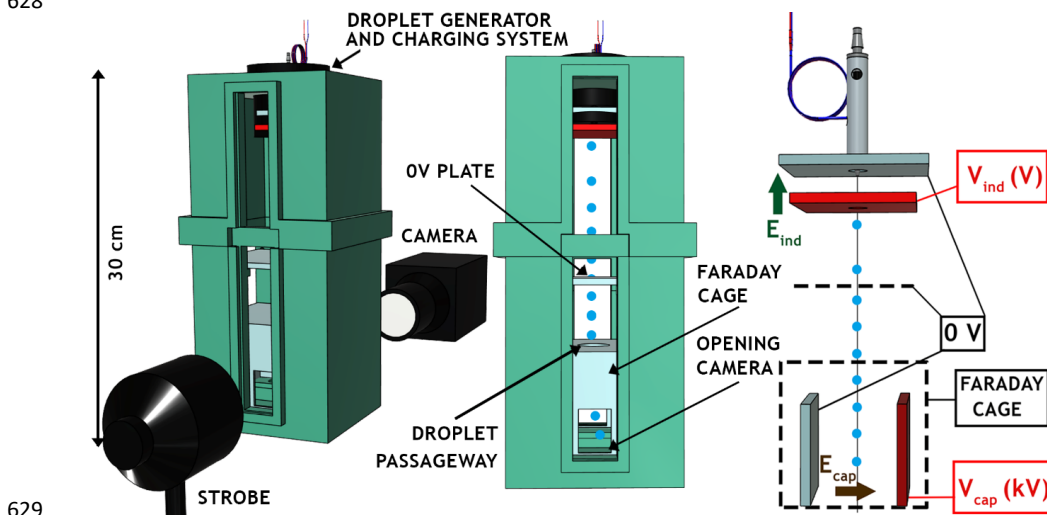
630 Figure 12 Setup to obtain the droplet charging relationship - (**Left** and **Center**) 3D view and (**Right**)
631 schema (not at scale)
632

633 **B.2   Droplet charge evaluation**
634 A series of 200 pictures pairs, with each one dephased from the other by a known time-step (Δt), are
635 obtained by optical shadowgraphy at the level of the capacitor. A circle Hough transform is then
636 applied to evaluate the droplet centers in every picture - an example is given in Figure 13 (Left)
637 where the two droplets from a picture are represented by two black crosses meanwhile the blue cross
638 is the detected droplet from the coupled picture dephased by Δt.
639

640 Then, the instantaneous droplet velocity $\overrightarrow{U_{D_0}(t)} = U_{D_0,x}\overrightarrow{u_x} + U_{\infty,A}\overrightarrow{u_y}$ at the first detected droplet
641 position (D_0) of coordinates (x_{D_0}, y_{D_0}) is calculated and the vertical velocity component ($U_{\infty,A}$)
642 determines the droplet radius (A) by reversing the Beard (1976) model. Here, the circle Hough
643 transform is not used to calculate the droplet radius since the camera zoom is at the lowest to get a
644 large field - the uncertainty would be too large.
645

646 Finally, the theoretical droplet trajectories at the capacitor are deduced by solving the 2nd Newton's
647 law where the buoyancy force (F_{buoy}), the drag force (F_{Drag}) and the electrostatic force ($F_{E_{cap}}$)
648 related to the electric field (E_{cap}) at the capacitor are considered, summarised in equations 9 :
649

$$\begin{cases} m_D \dfrac{d\boldsymbol{U}_D(t)}{dt} = \boldsymbol{F}_{buoy} + \boldsymbol{F}_{Drag} + \boldsymbol{F}_{E_{cap}} \\[2mm] \boldsymbol{F}_{buoy} = -m_D \dfrac{\rho_{water} - \rho_{air}}{\rho_{water}} g\, \boldsymbol{u}_y \\[2mm] \boldsymbol{F}_{Drag} = -\dfrac{C_D \pi \rho_{air} U_D^{\ 2} A^2}{2} \dfrac{\boldsymbol{U}_D(t)}{\|\boldsymbol{U}_D(t)\|} \\[2mm] \boldsymbol{F}_{E_{cap}} = Q E_{cap} \boldsymbol{u}_x \end{cases} \qquad (9)$$

650 With $\boldsymbol{U}_D$ - the instantaneous droplet velocity vector at the computational time t, ρ_{air} and ρ_{water} -
651 the air and water densities, g - the acceleration of gravity, m_D - the droplet mass, Q - the droplet
652 charge, C_D - the drag coefficient, $\boldsymbol{u}_x$ and $\boldsymbol{u}_y$ - the unit vectors in the cartesian coordinate system
653 visible in Figure 13 (Left).
654
655 By projecting on the corresponding axis, it is obtained the system of equations (10) to solve:

$$\begin{cases} m_D \dfrac{dU_{D,x}(t)}{dt} = Q E_{cap} - \dfrac{C_{D,x} \pi \rho_{air} U_{D,x}^{\ 2} A^2}{2} \\[2mm] m_D \dfrac{dU_{D,y}(t)}{dt} = -m_D \dfrac{\rho_{water} - \rho_{air}}{\rho_{water}} g - \dfrac{C_{D,y} \pi \rho_{air} U_{D,y}^{\ 2} A^2}{2} \end{cases} \qquad (10)$$

656 Where $C_{D,x}$ and $C_{D,y}$ are the drag coefficient projections depending on the Reynolds number
657 projections Re_x et Re_y in the cartesian coordinate system. Since $Re_x \ll 1$ et $Re_y < 2$ in the study, the
658 drag coefficient projections are calculated from the analytical expression given by Hinds (2012) and
659 summarised in equations (11):

$$\begin{cases} C_{D,x} = \dfrac{24}{Re_x} = \dfrac{12\, \eta_{air}}{A U_{D,x} \rho_{air}} \\[2mm] C_{D,y} = \dfrac{24}{Re_y} \underbrace{\left(1 + 0{,}15 Re_y^{\ 0{,}687}\right)}_{①} \approx \dfrac{12\, \eta_{air}}{A U_{D,y} \rho_{air}} \underbrace{\left(1 + 0{,}15 \left(\dfrac{2 A U_{\infty,A} \rho_{air}}{\eta_{air}}\right)^{0{,}687}\right)}_{=K_1} \end{cases} \qquad (11)$$

660 Note that the term ① in the Equations (11) is supposed as constant to simplify the resolution of the
661 equations (9) - giving second order differential equations. This assumption is justified since Re_y is
662 close to the unity and then $C_{T,y} = \dfrac{24}{Re_y}$ remains suitable. The equation system to solve becomes,
663 equations (12):

$$\begin{cases} m_D \dfrac{dU_{D,x}(t)}{dt} = Q E_{cap} - \overbrace{6\pi A \eta_{air}}^{K_2} U_{D,x} \\[2mm] m_D \dfrac{dU_{D,y}(t)}{dt} = -m_D \dfrac{\rho_{water} - \rho_{air}}{\rho_{water}} g - \underbrace{6\pi A \eta_{air} K_1}_{K_3} U_{D,y} \end{cases} \qquad (12)$$

664 After two consecutive integrations with the initial conditions - $U_{D,x}(t=0) = U_{D_0,x}$, $U_{D,y}(t=0) = U_{\infty,A}$,
665 $(x_D(t=0), y_D(t=0)) = (x_{D_0}, y_{D_0})$, the analytical equations of the horizontal and vertical droplet
666 positions, respectively referred as x_{th} and y_{th}, are given in equations (13):
667

$$\begin{cases} x_{th}(t) = \dfrac{Q E_{cap}}{K_2} t + \dfrac{m_D}{K_2}\left(U_{D_0,x} - \dfrac{Q E_{cap}}{K_2}\right)\left[1 - e^{-\frac{K_2}{m_D}t}\right] + x_{D_0} \\[3mm] y_{th}(t) = -\dfrac{m_D(\rho_{water} - \rho_{air})}{K_3 \rho_{water}} g t + \dfrac{m_D}{K_3}\left(U_{\infty,A} + \dfrac{m_D(\rho_{water} - \rho_{air})}{K_3 \rho_{water}} g\right)\left[1 - e^{-\frac{K_3}{m_D}t}\right] + y_{D_0} \end{cases}$$

$$(13)$$

668 Where $E_{cap} = -grad(V) = -\dfrac{V_{cap}}{0{,}01}$ V/m.
669
670 As presented in Figure 13 (Left), for every pair of pictures, the droplet charge (Q) is then evaluated
671 by looking for the theoretical droplet trajectory from the Equations (13) which fits the best with the
672 observed droplet positions. In the given example (Figure 13, Left), the fitted theoretical trajectory -
673 for V_{ind} = -32.25 V, V_{cap} = -629.5 V, A = 49.5 µm and the air temperature T_{air} = 292.55 K - illustrated
674 by the red line is obtained for a droplet charge (Q) of +9.10e+04 |e|. Finally, this method is applied

675 for the 200 picture pairs to get the mean droplet charge value - visible in Figure 13 (Right). Note that
676 the standard deviation of the 200 Q values gives the error bars in Figure 6.
677
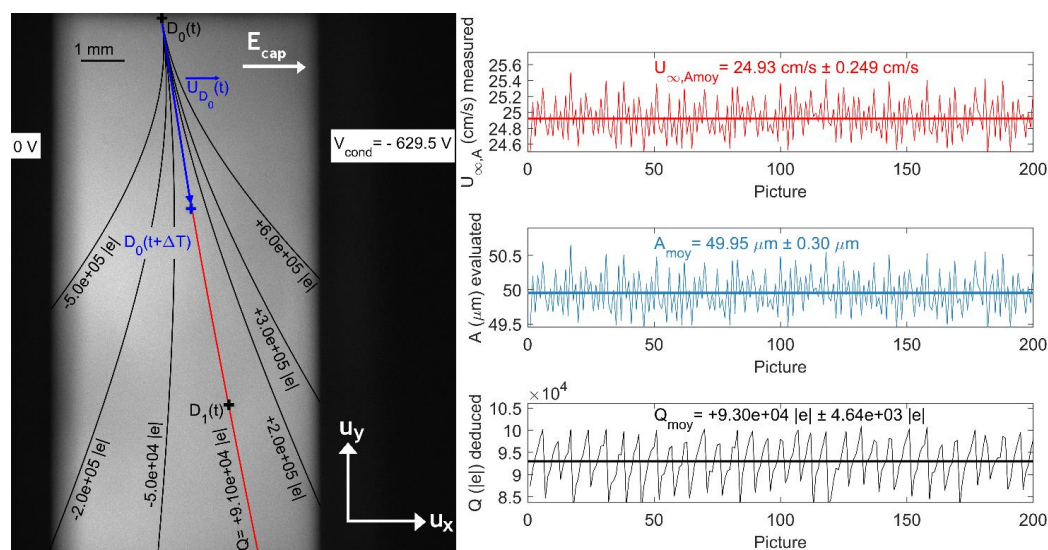
678
679 Figure 13 (**Left**) Determination of the theoretical droplet trajectory which fits the best with the
680 observed droplet positions - red line - and deduction of the droplet charge (Q). In this example,
681 V_{ind} = -32.25 V, V_{cap} = -629.5 V, A = 49.5 μm and the air temperature T_{air} = 292.55 K. (**Right, Top**)
682 Terminal velocity measurement, (**Right, Middle**) Droplet radius evaluation by reversing the Beard
683 (1976) model and (**Right, Bottom**) droplet charge deduction for a series of 200 pictures pairs. Mean
684 and standard deviations for the corresponding parameters are presented.

685
686 **B.3   Validation**
687 The method presented at the previous section is possible as long as the droplet has reached its
688 terminal velocity. As mentioned in **Dépée et at. (2020)** and visible in Figure 4 (Left) of the same
689 paper, droplets are generated at a velocity larger than their terminal velocity. It has been found that
690 a distance between the droplet generator and the capacitor of 15 cm was large enough to allow
691 droplets to reach their terminal velocity. In the setup in figure 12, this requirement prevails.

692
693 An experiment was performed to ensure that reversing the Beard (1976) model was a suitable method
694 to evaluated the droplet radius. For this purpose, the same droplet train was recorded in optical
695 shadowgraphy with a camera zoom at the lowest and at the greatest to respectively apply the Beard
696 (1976) model inversion and the circle Hough transform. In all tests, it was found a discrepancy of less
697 than 2 % between the two methods, giving overevaluations as well as underevaluations when
698 comparing one to the other.

699 Also, the disturbance of the electric field at the capacitor (E_{cap}) on the vertical droplet velocity was
700 studied. E_{cap} was then turned on and off to investigate the change in vertical droplet velocity. It was
701 found that during tests, E_{cap} reduced the vertical velocity up to 1.3 %. This situation was for a droplet
702 charge (Q) and a capacitor potential (V_{cap}) both negative. Some other tests also showed that the
703 droplet vertical velocity was increased up to 0.3 %, for a droplet charge and a capacitor potential of
704 unlike sign. Since these two extreme cases respectively represent a underevaluation of less than
705 0.7 % and an overestimation of less than 0.2 % of the droplet radius - this effect was neglected.

706 Finally, two other validations can be formulated by examining the Figure 6. First, several capacitor
707 potentials (V_{cap}) were used in the tests - from -629.5 to -477.4 V - giving the same charging
708 relationship. The Faraday Cage is consequently reliable, there is not impact of the electric field
709 (E_{cap}) on the droplet charge. Secondly, in the four tests the droplet radius varies from 47.0 to
710 51.2 μm. Thus, the droplet charging system is independent of the droplet size and droplet
711 evaporation.

References

Barlow, A. K., & Latham, J. (1983). A laboratory study of the scavenging of sub-micron aerosol by charged raindrops. Quarterly Journal of the Royal Meteorological Society, 109(462), 763-770.

Beard, K. V. (1974). Experimental and numerical collision efficiencies for submicron particles scavenged by small raindrops. Journal of the Atmospheric Sciences, 31(6), 1595-1603.

Beard, K. V. (1976). Terminal velocity and shape of cloud and precipitation drops aloft. Journal of the635 Atmospheric Sciences, 33(5), 851-864.

Byrne, M. A., & Jennings, S. G. (1993). Scavenging of sub-micrometre aerosol particles by water drops. Atmospheric Environment. Part A. General Topics, 27(14), 2099-2105.

Clement, C. F., & Harrison, R. G. (1992). The charging of radioactive aerosols. Journal of aerosol science, 23(5), 481-504.

Crouse, D. L., Peters, P. A., van Donkelaar, A., Goldberg, M. S., Villeneuve, P. J., Brion, O., & Brauer, M. (2012). Risk of nonaccidental and cardiovascular mortality in relation to long-term exposure to low concentrations of fine particulate matter: a Canadian national-level cohort study. Environmental health perspectives, 120(5), 708-714.

Dépée, A., Lemaitre, P., Gelain, T., Monier, M., & Flossmann, A. (2019). Laboratory study of collection efficiency of submicron aerosol particles by cloud droplets. Part I - Influence of relative humidity.

Flossmann, A. I., Hall, W. D., & Pruppacher, H. R. (1985). A theoretical study of the wet removal of atmospheric pollutants. Part I: The redistribution of aerosol particles captured through nucleation and impaction scavenging by growing cloud drops. *Journal of the Atmospheric Sciences*, *42*(6), 583-606.

Flossmann, A. I. (1998). Interaction of aerosol particles and clouds. *Journal of the atmospheric sciences*, *55*(5), 879-887.

Greenfield, S. M. (1957). Rain scavenging of radioactive particulate matter from the atmosphere. *Journal of Meteorology*, *14*(2), 115-125.

Grover, S. N., & Beard, K. V. (1975). A numerical determination of the efficiency with which electrically charged cloud drops and small raindrops collide with electrically charged spherical particles of various densities. *Journal of the Atmospheric Sciences*, *32*(11), 2156-2165.

Hinds, W. C. (2012). Aerosol technology: properties, behavior, and measurement of airborne particles. John Wiley & Sons.

Jackson, J. D. (1999). Classical Electrodynamics.

Jaworek, A., Adamiak, K., Balachandran, W., Krupa, A., Castle, P., & Machowski, W. (2002). Numerical simulation of scavenging of small particles by charged droplets. Aerosol Science & Technology, 36(9), 913-924.

Kraemer, H. F., & Johnstone, H. F. (1955). Collection of aerosol particles in presence of electrostatic fields. Industrial & Engineering Chemistry, 47(12), 2426-2434.

Laguionie, P., Roupsard, P., Maro, D., Solier, L., Rozet, M., Hébert, D., & Connan, O. (2014). Simultaneous quantification of the contributions of dry, washout and rainout deposition to the total deposition of particle-bound 7Be and 210Pb on an urban catchment area on a monthly scale. *Journal of Aerosol Science*, *77*, 67-84.

Lai, K. Y., Dayan, N., & Kerker, M. (1978). Scavenging of aerosol particles by a falling water drop. Journal of the Atmospheric Sciences, 35(4), 674-682.

771 Pauthenier, M., & Moreau-Hanot, M. (1932). La charge des particules sphériques dans un champ
772 ionisé.

774 Reischl, G. P. W. W., John, W., & Devor, W. (1977). Uniform electrical charging of monodisperse
775 aerosols. *Journal of Aerosol Science*, *8*(1), 55-65.

777 Twomey, S. (1974). Pollution and the planetary albedo. *Atmospheric Environment (1967)*, *8*(12), 1251-
778 1256.

780 Takahashi, T. (1973). Measurement of electric charge of cloud droplets, drizzle, and raindrops. *Reviews
781 of Geophysics*, *11*(4), 903-924.

783 Tinsley, B. A., Rohrbaugh, R. P., Hei, M., & Beard, K. V. (2000). Effects of image charges on the
784 scavenging of aerosol particles by cloud droplets and on droplet charging and possible ice nucleation
785 processes. Journal of the atmospheric sciences, 57(13), 2118-2134.

787 Tinsley, B. A., Zhou, L., & Plemmons, A. (2006). Changes in scavenging of particles by droplets due to
788 weak electrification in clouds. Atmospheric Research, 79(3), 266-295.

790 Tinsley, B. A., & Zhou, L. (2015). Parameterization of aerosol scavenging due to atmospheric
791 ionization. *Journal of Geophysical Research: Atmospheres*, *120*(16), 8389-8410.

793 Unger, L. (2001). *Charge d'aérosol par décharge électrique pour la filtration d'effluents
794 particulaires* (Doctoral dissertation, Paris 11).

796 Unger, L., Boulaud, D., & Borra, J. P. (2004). Unipolar field charging of particles by electrical discharge:
797 effect of particle shape. *Journal of Aerosol Science*, *35*(8), 965-979.

799 Wang, P. K., & Pruppacher, H. R. (1977). An experimental determination of the efficiency with which
800 aerosol particles are collected by water drops in subsaturated air. Journal of the Atmospheric Sciences,
801 34(10), 1664-1669.

803 Wang, H. C., Leong, K. H., Stukel, J. J., & Hopke, P. K. (1983). Collection of hydrophilic and hydrophobic
804 charged submicron particles by charged water droplets. Journal of aerosol science, 14(6), 703-712.
805